Nanoscale Advances

ROYAL SOCIETY OF CHEMISTRY

PAPER

View Article Online
View Journal | View Issue



Cite this: *Nanoscale Adv.*, 2021, **3**, 575

# Theoretical insights into C–H bond activation of methane by transition metal clusters: the role of anharmonic effects†

Preeti Bhumla, * Manish Kumar and Saswata Bhattacharya *

In heterogeneous catalysis, the determination of active phases has been a long-standing challenge, as materials' properties change under operational conditions (*i.e.* temperature (*T*) and pressure (*p*) in an atmosphere of reactive molecules). As a first step towards materials design for methane activation, we study the *T* and *p* dependence of the composition, structure, and stability of metal oxide clusters in a reactive atmosphere at thermodynamic equilibrium using a prototypical model catalyst having wide practical applications: free transition metal (Ni) clusters in a combined oxygen and methane atmosphere. A robust methodological approach is employed, where the starting point is systematic scanning of the potential energy surface (PES) to obtain the global minimum structures using a massively parallel cascade genetic algorithm (cGA) at the hybrid density functional level. The low energy clusters are further analyzed to estimate their thermodynamic stability at realistic *T*, $p_{O2}$ and $p_{CH4}$ using *ab initio* atomistic thermodynamics (*ai*AT). To incorporate the anharmonicity in the vibrational free energy contribution to the configurational entropy, we evaluate the excess free energy of the clusters numerically by a thermodynamic integration method with *ab initio* molecular dynamics (*ai*MD) simulation inputs. By analyzing a large dataset, we show that the conventional harmonic approximation miserably fails for this class of materials, and capturing the anharmonic effects on the vibration free energy contribution is indispensable. The latter has a significant impact on detecting the activation of the C–H bond, while the harmonic infrared spectrum fails to capture this, due to the wrong prediction of the vibrational modes.

Received 13th August 2020
Accepted 16th November 2020

DOI: 10.1039/d0na00669f

rsc.li/nanoscale-advances



## 1 Introduction

Methane is the primary component of natural gas, which is one of the simplest, nearly ubiquitous, low-cost, clean and easily extractable energy sources found in nature.[1–6] Additionally, methane is also a prominent greenhouse gas. Therefore, it is highly desirable to convert methane into valuable products.[7] Synthesis gas (syngas, a mixture of CO and $H_2$) production from methane is an important route for the effective utilization of abundant natural gas in producing methanol, liquid hydrocarbons, ammonia and dimethyl ether.[8–10] The efficient activation of methane has been a major challenge as C–H bonds in methane possess high bond strength (4.5 eV), low polarizability and negligible electron affinity making it a least reactive hydrocarbon.[11–13] Since methane is extremely inert, its conversion to chemical products is difficult. To circumvent this problem, a suitable catalyst must be developed. Hence, the catalytic conversion of methane is one of the most appealing fields of study in both academia and industry.[14–26]

Numerous experimental and theoretical studies have established that the reactivity of small metal clusters (as catalysts) in the gas phase varies with the number of atoms.[20,27–30] It has been found that reducing particle size in the cluster reveals the possibility of several interesting size effects.[31–34] Particularly, transition metal (TM) clusters are well known for their efficient homogeneous and heterogeneous catalytic activity.[35–40] This is primarily ascribed to the presence of partially occupied d-shells, which assist in exhibiting multiple oxidation states in their complexes.[32,41–43] Note that the properties of a material change substantially in the operational environment, particularly in an atmosphere of reactive molecules. Under reaction conditions, the catalyst consists of a wide range of structures including different numbers of atoms with various oxidation states, all of which could be active to some extent in the catalytic reaction. As a result, some inevitable questions arise naturally, *e.g.*, "what are the species present in the real catalyst and what are their structures?", and "how do those catalysts change their structure and catalytic properties upon adsorption of different ligand molecules?".

In order to address the above questions in the context of heterogeneous catalysis, one of the most important aspects is to

*Department of Physics, Indian Institute of Technology Delhi, New Delhi, India. E-mail: Preeti.Bhumla@physics.iitd.ac.in; saswata@physics.iitd.ac.in; Fax: +91 11 2658 2037; Tel: +91 11 2659 1359*

† Electronic supplementary information (ESI) available: Details of choice of functionals, temperature control using Nose–Hoover thermostat, contribution of $F_{vib}$ at different temperatures, thermodynamic integration and probability of occurence of different configurations. See DOI: 10.1039/d0na00669f

identify the active species and to determine the structure of the catalyst.[44] In light of this, there is a justified need to provide theoretical guidance to experiments on the stoichiometry and stability of the clusters under realistic conditions, *i.e.* at a finite temperature ($T$) and pressure ($p$). To better understand the situation theoretically, we consider a prototypical model system of nickel ($Ni_4$, which has already been experimentally synthesized and has high selectivity[45–47]) in a reactive atmosphere of $O_2$ and $CH_4$ gas molecules under realistic conditions. Note that Ni-based catalysts, owing to their low cost, high selectivity and high activity, have been extensively employed experimentally in catalysis in the past.[48–53] Typically, in the presence of a reactive atmosphere, clusters adsorb surrounding gas molecules and form intermediate phases $[Ni_4O_x(CH_4)_y]$ at thermodynamic equilibrium. The latter generally proves to be an active material for various applications in the field of heterogeneous catalysis. However, determining such stable phases (stoichiometries) theoretically has never been an easy task. This requires a comprehensive understanding of all the possible structures of $[Ni_4O_x(CH_4)_y]$ and their thermodynamic stability at a given $T$ and $p$. This demands a robust methodological approach that integrates various levels of theory combined into one multi-scale simulation.[54] Moreover, at a finite temperature, anharmonicity may play a role in molecular vibrations and quantum oscillations. The atoms in a molecule or a solid vibrate around their equilibrium positions. At low temperature, when these vibrations have smaller amplitudes, they can be described by harmonic oscillators. However, when the vibrational amplitudes are large, for example at high temperatures, anharmonicity becomes important. Studying vibrating anharmonic systems using quantum mechanics is a computationally demanding task because anharmonicity not only makes the potential experienced by each atom (oscillator) complicated, but also introduces coupling between the oscillators. It is, therefore, more feasible to use first-principles methods such as those within the framework of density functional theory (DFT)[55,56] to map the anharmonic potential experienced by the atoms. Accurate anharmonic vibrational energies can then be obtained numerically from first-principles calculations. This helps in determining the correct thermodynamic stability of the active species (*i.e.* catalysts) responsible for driving a favourable reaction kinetics.

In this article, we have investigated the role of environment [*i.e.*, temperature ($T$), partial pressure of oxygen ($p_{O2}$) and partial pressure of methane ($p_{CH4}$)] to understand the thermodynamic stability of different configurations of $Ni_4O_x(CH_4)_y$ ($0 \le x \le 8$, $0 \le y \le 3$) clusters in a reactive atmosphere of $O_2$ and $CH_4$ molecules. As a first step, a systematic scanning of the potential energy surface (PES) is done *via* a cascade genetic algorithm (cGA)[57–59] approach to obtain the global minimum (GM) configurations of $Ni_4O_x(CH_4)_y$ clusters. Subsequently, we employ *ab initio* atomistic thermodynamics (*ai*AT)[57,60,61] in the framework of DFT to determine the thermodynamic stability of those configurations under operational conditions. To incorporate the anharmonicity in the vibrational free energy contribution to the configurational entropy, we evaluate the excess free energy of the clusters numerically by a thermodynamic integration method[62] with *ab initio* molecular dynamics (*ai*MD) simulation inputs. By analyzing a large dataset, we try to establish the important contribution of vibrational free energy to predict potential catalysts for C–H bond activation. We have thoroughly addressed the contribution of vibrational free energy using harmonic approximation and compared the same after inclusion of anharmonic effects at a moderately high temperature (relevant for the catalysis). We further validate our findings through infrared (IR) spectrum analysis.

## 2 Methodology

We proceed very systematically to solve this problem – (i) the first step is an extensive and efficient scanning of the potential energy surface (PES) by an efficient well-established global structure optimization procedure; (ii) subsequently, the influence of the experimental conditions (here, temperature and pressure of a reactive atmosphere) is included. For the latter, we have shown three suites of three different approaches to establish the importance of accurate estimation of the contribution of free energy of vibration in determining the thermodynamic stability of the concerned material.

### 2.1 Efficient scanning of the potential energy surface

As a first step, we have generated a large data set of $Ni_4O_x(CH_4)_y$ ($0 \le x \le 8$, $0 \le y \le 3$) clusters. Here, we have varied the value of $x$ and $y$ ($x$ = no. of oxygen atoms, $y$ = no. of $CH_4$ molecules) from zero to the saturation value, which means that $x$ and $y$ values are increased with all possible combinations until no more O atoms/$CH_4$ molecules can be adsorbed by the cluster. To do this, we used a massively parallel cascade genetic algorithm (cGA) to thoroughly scan the PES in determining all possible low-energy structures including the global minimum (GM).[57–59] GA is a global optimization technique based on the principles of natural evolution. In general, this algorithm includes the following steps – an initial population is formed with a group of individuals, created as absolutely random. The individuals in the running population are then evaluated *via* a fitness function, *i.e.* lower energy structures have a higher fitness function and *vice versa*. This algorithm aims to optimize this (scalar) fitness function. Two individuals (*i.e.* structures) are then selected at random, with their respective weights based on their fitness – *i.e.* the higher the fitness, the higher the chance of being selected. These individuals then 'mate', *i.e.*, they are combined to create one candidate offspring that can in turn be 'mutated' randomly. In the next selection for 'mating', this new individual is included in the pool of candidates and can be selected on the basis of its fitness. This algorithm continues until a convergence criterion is met.‡

‡ First, we have provided typically about 50–100 random structures in the initial pool of cGA to start the scanning. Clusters with more atoms were scanned for more isomers owing to their more complex PES to determine the GM structure. Typically, for a PES with 15+ atoms, we have scanned about 800–1000 structures. However for a system with less than 10 atoms, we could figure out the minimum after scanning ~500 structures. For even smaller clusters (less than 5 atoms), this number is even smaller. We have taken the best 20–30 structures having low energies from the total pool of structures within a 1 eV energy window for further post processing to confirm the stable conformers separately.

The term "cascade" means a multi-stepped algorithm, where successive steps employ a higher level of theory and each succeeding level takes information obtained at its immediate lower level. Typically, a cGA algorithm starts with a classical force field and goes up to density functional theory (DFT) with hybrid exchange and correlation ($\varepsilon_{xc}$) functionals. Note that the prototypical model system that we have chosen here is a representative of a class of systems for which very accurate evaluation of the PES is mandatory for meaningful experimental predictions. Incidentally, we have already explained that hybrid $\varepsilon_{xc}$ functionals are required[58] since, as we have reported, the PBE $\varepsilon_{xc}$ functional[63] highly overestimates the stability of clusters containing larger concentrations of O atoms.[30,44,58,64] This results in a qualitatively wrong prediction of $O_2$ adsorption for O-rich cases. Such behavior is not confirmed by more advanced hybrid $\varepsilon_{xc}$ functionals [*e.g.* HSE06,[65] PBE0[66]]. Moreover, the spin states of the clusters are also different as found by PBE and PBE0/HSE06 $\varepsilon_{xc}$ functionals. However, doing everything at the level of high-accuracy hybrid $\varepsilon_{xc}$ functionals is computationally very expensive. This is why a hierarchical scheme for an efficient scanning of the PES (starting from a classical force field and going up to DFT with hybrid $\varepsilon_{xc}$) is thoroughly benchmarked and proposed in order to avoid wasting time and computational resources with high-accuracy calculations in uninteresting regions of the configurational phase space [see details in ref. 57–59].

In view of this, in this cascade GA algorithm, after preparing a crude database of structures using GA at the level of classical force field (ReaxFF), we start our DFT-GA. In DFT-GA, we optimize the structures with PBE but the energetics are computed with an advanced hybrid $\varepsilon_{xc}$ functional to evaluate the fitness function of the cluster correctly. This is due to the reason that in optimization of the structures, we basically compute the forces amongst atoms, which are determined by the gradient of energy *i.e.* precisely the differences of energies in order to compute the derivatives. As a result, the electron's self-interaction error present in the PBE $\varepsilon_{xc}$ functional gets canceled out. Therefore, there is not much difference in the structures that we get from PBE and/or HSE06 $\varepsilon_{xc}$ functionals. In addition, the HSE06 $\varepsilon_{xc}$ functional is computationally much more expensive than the PBE $\varepsilon_{xc}$ functional making the PBE $\varepsilon_{xc}$ functional an efficient choice for structural optimization in our system. However, to evaluate the fitness function PBE energetics cannot be used. Thus we need to perform additional single point energy calculations at the level of hybrid $\varepsilon_{xc}$ on top of the PBE optimized structure. We have incorporated all these settings in cGA implementation. For details of this cGA implementation, accuracy and validation, we recommend our previous studies as given in ref. 57–59.

All DFT calculations are performed using the FHI-aims code, employing an all-electron code with numerical atom centered basis sets.[67] Considering the fact that first-principles based calculations are computationally demanding, lighter (*viz.* light settings with a tier 2 basis set[67]) DFT settings are implemented in the cGA to find the global minimum structures. The atomic zero-order regular approximation (ZORA) is used for the scalar relativistic correction.[68] The vdW correction is calculated according to the Tkatchenko–Scheffler scheme.[69] The low energy structures obtained from the cGA are further optimized with PBE at higher level settings (*viz.* tight settings with a tier 2 basis set[67]). The atomic forces are converged up to $10^{-5}$ eV Å$^{-1}$. Finally, the total single point energy is calculated on top of this optimized structure using the HSE06 hybrid $\varepsilon_{xc}$ functional (see further details for validation of $\varepsilon_{xc}$ functionals in Section I in the ESI†).

### 2.2 Accurate estimation of free energy of formation

After the cGA search is completed, with each of these selected structures (within an energy window of 1 eV from the GM), we have performed calculations of the harmonic vibrations using finite differences of the analytic forces. This step is necessary to achieve the following two objectives. The immediate purpose is to identify the unstable structures, *i.e.*, those having imaginary vibrational frequencies. The other objective is to note down the frequencies to determine the vibrational free energy ($F_{vib}$)[57,60] within harmonic approximations. Next, to capture the anharmonic effects using a thermodynamic integration method,[62] we have carried out *ab initio* molecular dynamics (*ai*MD) simulations for 8 ps each at different temperatures *viz.* $T = 50$ K, 100 K, 300 K, 600 K and 800 K in a canonical ensemble (*i.e.*, one with constant temperature and volume). We have employed the velocity Verlet scheme[70] for the integration of Newtonian equations with a time-step of 1 fs and the temperature of the system is controlled using the Nose–Hoover thermostat[71] (for details see Section II in the ESI†). In the following section this whole procedure is explained in steps to determine the thermodynamically stable components at different levels of accuracy to estimate the free energy of formation of the candidate structures under realistic conditions.

### 2.3 Determination of stable phases of the $[Ni_4O_x(CH_4)_y]$ clusters

After obtaining all low energy isomers corresponding to different configurations of $Ni_4O_x(CH_4)_y$ clusters from cGA, we study their thermodynamic stability under realistic conditions using the *ai*AT approach. Here, we assume that there is an exchange of atoms between the system ($Ni_4$ cluster) and the surroundings (consisting of $O_2$ and $CH_4$ gas molecules) at finite temperatures and pressures, *via* the following reaction:

$$Ni_4 + \frac{x}{2}O_2 + yCH_4 \rightleftharpoons Ni_4O_x(CH_4)_y \quad (1)$$

Note that adsorption and desorption of $O_2$, $H_2$, $H_2O$ and $CO_2$ moieties are also taken into account by cGA, where all sorts of mutation and crossover operations take place giving rise to all possible structural moieties. Therefore even if the configuration stoichiometrically reads as $Ni_4O_x(CH_4)_y$, it does include all possible moieties.

The Gibbs free energy of formation ($\Delta G$) of all the $Ni_4O_x(CH_4)_y$ structures is then evaluated as a function of $T$, $p_{O2}$ and $p_{CH4}$ by applying *ai*AT. The composition (for a particular value of $x$ and $y$) having the minimum Gibbs free energy of formation is most likely to be found in the experiments at a specific $T$, $p_{O2}$

and $p_{CH4}$. $\Delta G(T,p)$ is therefore calculated as per the following equation:

$$\Delta G(T,p_{O2},p_{CH4}) = F_{Ni4Ox(CH4)y}(T) - F_{Ni4}(T) - x \times \mu_O(T,p_{O2}) - y \times \mu_{CH4}(T,p_{CH4}) \quad (2)$$

where $F_{Ni4Ox(CH4)y}(T)$ and $F_{Ni4}(T)$ are the Helmholtz free energies of the cluster + ligands $[Ni_4O_x(CH_4)_y]$ and the pristine $[Ni_4]$ cluster, respectively. $x$ and $y$ represent the number of oxygen atoms and methane molecules that are exchanged with the environment in the reactive atmosphere, respectively.

The Helmholtz free energies $F_{Ni4Ox(CH4)y}(T)$ and $F_{Ni4}(T)$ consist of the respective total DFT energy along with their free energy contributions from translational, rotational, vibrational, symmetry and spin-degeneracy terms.[57,60] The contributions of different terms in the expression of Helmholtz free energies $F$ are given as follows:[57]

$$F = F_{trans} + F_{rot} + F_{vib} + F_{symm} + F_{spin} + E^{DFT} \quad (3)$$

$$F_{trans} = -\frac{3}{2}k_B T \ln\left[\left(\frac{2\pi m}{h^2}k_B T\right)\right] \quad (4)$$

$$F_{rot} = -k_B T \ln\left[8\pi^2\left(\frac{2\pi k_B T}{h^2}\right)^{\frac{3}{2}}\right] - \frac{1}{2}k_B T \ln(I_A I_B I_C) \quad (5)$$

$$F_{vib}^{harmonic} = \sum\frac{h\nu}{2} + \sum k_B T \ln\left[1 - \exp\left(-\frac{h\nu}{k_B T}\right)\right] \quad (6)$$

where the summation runs over all the vibrational modes of the concerned structure. $I_A$, $I_B$ and $I_C$ are the moments of inertia of the structure along $a$, $b$ and $c$ axes.

$$F_{symmetry} = k_B T \ln \sigma \quad (7)$$

$$F_{spin} = -k_B T \ln \mathcal{M} \quad (8)$$

where $\sigma$ is the symmetry number and $\mathcal{M}$ is the spin multiplicity. $k_B$, $h$, and $E^{DFT}$ are respectively the Boltzmann constant, Planck constant, and total DFT energy.

It has been noticed that the total DFT energy is the dominant term, which is evaluated in its ground state configuration with respect to both geometry and spin state. The rest of the terms, except the contribution from the vibrational degrees of freedom ($F_{vib}$), are usually considered as invariant since they do not change much (and even if they change, the order is insignificant) due to the dependence on most of the constant terms *viz.* mass, moment of inertia, universal constants, *etc.* However, the vibrational contribution is dependent on the frequencies of vibration, which are unique for a given structure. Thus, the Helmholtz free energy can be written as follows:

$$F(T) = E^{DFT} + F_{vib} + \Delta \quad (9)$$

where $\Delta$ is considered to be a constant term. At low temperature, $F_{vib}$ usually contributes 1–5% for a small cluster of few atoms (for detailed contribution of $F_{vib}$ at different temperatures, see Section III in the ESI†). Thus, while computing $\Delta G(T,p)$, since we take differences of two free energy expressions (*i.e.* a system with ligands and a system without ligands), we assume this to be very small and therefore, it can be neglected. However, there exist some systems where $F_{vib}$ contributes significantly even after taking the difference of two such terms to compute $\Delta G(T,p)$.[72] In view of this, though a significant number of studies have neglected $F_{vib}$, it is not recommended. Here, we estimate the role of $F_{vib}$ *via* state-of-the-art theoretical techniques at various levels of accuracy. $\mu_O(T,p_{O2})$ and $\mu_{CH4}(T,p_{CH4})$ represent the chemical potential of an oxygen atom $\left(\mu_O = \frac{1}{2}\mu_{O_2}\right)$ and a methane molecule, respectively. The relation of $\mu_O(T,p_{O2})$ with $T$ and $p_{O2}$ is governed by the ideal (diatomic) gas approximation. The expression is as follows:[57]

$$\begin{aligned}\mu_{O_2}(T,p_{O_2}) = &-k_B T \ln\left[\left(\frac{2\pi m}{h^2}\right)^{\frac{3}{2}}(k_B T)^{\frac{5}{2}}\right] \\ &+k_B T \ln p_{O_2} - k_B T \ln\left(\frac{8\pi^2 I_A k_B T}{h^2}\right) \\ &+\frac{h\nu_{OO}}{2} + k_B T \ln\left[1 - \exp\left(-\frac{h\nu_{OO}}{k_B T}\right)\right] \\ &+E^{DFT}(O_2) - k_B T \ln \mathcal{M} + k_B T \ln \sigma\end{aligned} \quad (10)$$

For the $CH_4$ molecule, $I_A = I_B = I_C = I$, and therefore,

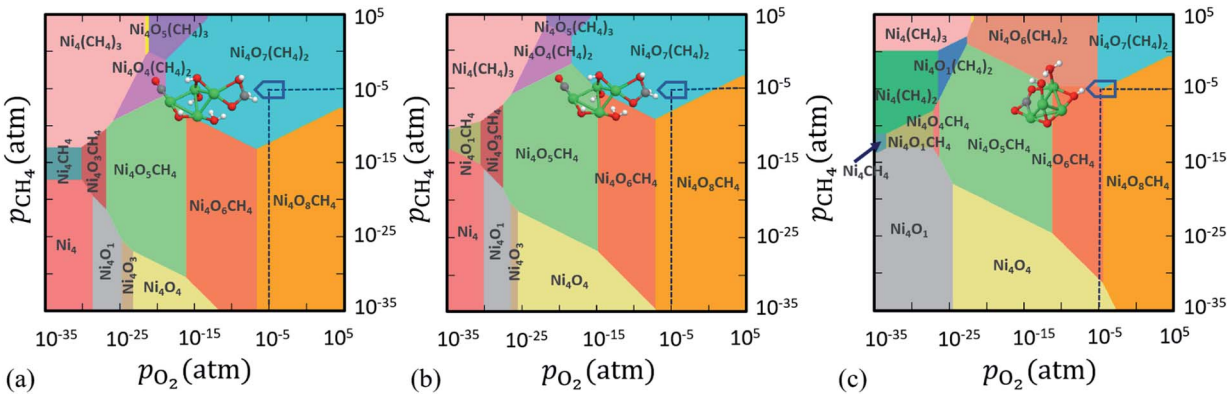


Fig. 1 2D projection of the 3D phase diagram obtained for $Ni_4O_x(CH_4)_y$ clusters in the reactive atmosphere of $O_2$ and $CH_4$. In this plot $\Delta G(T,p)$ is computed when (a) only DFT total energies are included, (b) DFT + $F_{vib}^{harmonic}$ are included and (c) DFT + $F_{vib}^{anharmonic}$ are included to compute $F(T)$ of the respective configurations as shown in eqn (2). Colored regions show the most stable compositions in a wide range of pressure at $T = 800$ K.

$$\mu_{CH_4}(T, p_{CH_4}) = -k_B T \ln\left[\left(\frac{2\pi m}{h^2}\right)^{\frac{3}{2}}(k_B T)^{\frac{5}{2}}\right] + k_B T \ln p_{CH_4} - k_B T \ln\left[8\pi^2\left(\frac{2\pi I k_B T}{h^2}\right)^{\frac{3}{2}}\right] + \sum\frac{h\nu_{CH}}{2} + \sum k_B T \ln\left[1 - \exp\left(-\frac{h\nu_{CH}}{k_B T}\right)\right] + E^{DFT}(CH_4) - k_B T \ln \mathscr{M} + k_B T \ln \sigma \quad (11)$$

Using eqn (2), we have obtained the 3D phase diagram ($p_{O2}$ *vs.* $p_{CH4}$ *vs.* $\Delta G(T,p)$) at an experimentally relevant $T$ (here, 800 K). The 2D projection of this 3D phase diagram is shown in Fig. 1 after aligning the negative $\Delta G(T,p)$ axis to be vertically up. We have considered all the configurations of $Ni_4O_x(CH_4)_y$ clusters. Note that only those phases that minimize the $\Delta G(T,p)$ at a specific $p_{O2}$, $p_{CH4}$ and $T = 800$ K are visible in Fig. 1. Each color in the phase diagram represents a stable configuration of the catalyst. All the phase diagrams are constructed at $T = 800$ K as it is a suitable temperature for methane activation.

# 3 Results

## 3.1 Comparing the role of $F_{vib}$ in $\Delta G(T,p)$: importance of capturing anharmonic effects

Herein, we have implemented a suite of three state-of-the-art techniques to compute $\Delta G(T,p)$. The first one is without any explicit contribution of $F_{vib}$ (as in eqn (9)), *i.e.* only the total DFT energy ($E^{DFT}$) of the cluster with and without ligands is considered (see Fig. 1a). In the second case, we duly consider $F_{vib}$ but up to harmonic approximation to calculate $\Delta G(T,p)$. $F_{vib}^{harmonic}$ is computed using eqn (6). Note that after adding $F_{vib}^{harmonic}$ with $E^{DFT}$ (as in eqn (9)), a new phase is introduced along with slight rearrangement of the existing phases, especially near the boundary region of competing configurations (see Fig. 1b). However, despite some small changes in Fig. 1a and b, we do not see any significant difference to identify the most stable phases in the experimentally realistic pressure range. In this region, $Ni_4O_6CH_4$, $Ni_4O_7(CH_4)_2$ and $Ni_4O_8CH_4$ are the stable phases and if we look at the region where $p_{O2} = p_{CH4} = 10^{-5}$ atm ($T = 800$ K), $Ni_4O_7(CH_4)_2$ turns out to be the most stable phase (see Fig. 1a and b), irrespective of whether $F_{vib}^{harmonic}$ is taken into consideration or not.

Now here, it is assumed that at $T = 800$ K, the oscillations are constrained to vibrate at a harmonic potential. However, the real system does not necessarily follow this assumption. And if so, the real anharmonic potential can be very different from the harmonic potential. In such case, the expression for $F_{vib}$ can vary from one configuration to the other.

Therefore, in an attempt to refine the expression of $\Delta G(T,p)$ at finite $T,p$, we include anharmonic effects in the PES (see Fig. 1c). In order to quantitatively account for the anharmonic effects, we perform the thermodynamic integration[62] taking input from *ai*MD simulations to evaluate the excess free energy of clusters. Here, we have assumed that at low $T$ (*e.g.* 10 K), neither harmonic nor anharmonic potentials diverge much. Taking such low $T$ as our reference state, the Helmholtz free energy $F(T)$ is calculated according to the following equation (for a detailed derivation, see Section IV in the ESI†):

$$F(T) = \underbrace{E^{DFT} + U^{ZPE}}_{U^{ref}} + \frac{T}{T_0}F_{vib}^{harmonic}(T_0) - \underbrace{T\int_{T_0}^{T}\frac{dT}{T^2}\left(\langle U\rangle_T - U^{ref}\right)}_{\text{thermodynamic integration}} - k_B T\frac{N}{2}\ln\frac{T}{T_0} \quad (12)$$

where $T_0$ and $T$ represent the initial and final temperatures, respectively. $E^{DFT}$, $U^{ref}$, $F_{vib}^{harmonic}(T_0)$, $N$ and $\langle U\rangle_T$ are respectively the total DFT energy, zero point energy, Helmholtz free energy at temperature $T_0$ (10 K) under harmonic approximation, total number of atoms and canonical average of the total energy at temperature $T$ (800 K) of the clusters. We have run the *ai*MD simulations in the canonical ensemble for 8 ps at five different temperatures, from $T = 10$ K to $T = 800$ K, to obtain the average energy ($\langle U\rangle_T$). After that, we have performed quadratic curve fitting for this dataset and numerically integrated the corresponding function over the limits $T_0 = 10$ K to $T = 800$ K to get the value of $F(T)$ at $T = 800$ K. After evaluating $F(T)$, we have minimized $\Delta G(T,p)$ using the same aforementioned procedure and obtained the phase diagram with the anharmonic effects (see Fig. 1c). Interestingly, we notice that a completely new phase *viz.* $Ni_4O_6(CH_4)_2$ appears to be stable alongside the three existing phases [*viz.* $Ni_4O_6CH_4$, $Ni_4O_8CH_4$ and $Ni_4O_7(CH_4)_2$] under reaction conditions ($p_{O2} = p_{CH4} = 10^{-5}$ atm and $T = 800$ K). On comparing Fig. 1a–c, we conclude that not only have the stable phases been destabilized erroneously but also the new phases have a high probability of being missed under reaction conditions, if the anharmonic effects are not taken into consideration for this class of materials. Hence, it indicates that the inclusion of anharmonicity in these clusters affects the thermodynamic stability under operational conditions.

To clearly examine the relative probability of all the competing isomers simultaneously, we have estimated the probability of occurrence of all (meta)stable phases using all three methods (*viz.* DFT, DFT + $F_{vib}^{harmonic}$ and DFT + $F_{vib}^{anharmonic}$) under different reaction conditions. It is calculated using the following equation (see the detailed derivation in Section V of the ESI†):

$$\frac{N_n}{N} = \frac{\exp(\beta\Delta G_n)}{1 + \sum_m \exp(\beta\Delta G_m)} \quad (13)$$

Here, we assume that a total of $N$ different configurations are possible out of which $N_n$ is the number of a given type (say n) and its occurrence is given as per Fermi–Dirac statistics. Thus $\frac{N_n}{N}$ is the probability of occurrence of the type-n configuration.[73] $\Delta G_n$ is the Gibbs free energy of formation of the type-n configuration. As the range of $\frac{N_n}{N} \times 100\%$ is significantly large, we have taken the logarithm of the above equation in the plots (see Fig. 2). Therefore, the maximum possible value on the $y$-axis is ~2 when $N_n \approx N$; *i.e.* type-n is the most dominant configuration. In Fig. 2a, we can clearly see by all three methods that the

first structure [*viz.* $Ni_4O_7(CH_4)_2$] is most likely to be stable. But after that, for the next three structures (*viz.* $Ni_4O_8CH_4$, $Ni_4O_6CH_4$ and $Ni_4O_6(CH_4)_2$), DFT + $F_{vib}^{harmonic}$ and DFT + $F_{vib}^{anharmonic}$ work counter to each other. Moreover, if we see Fig. 2b, the situation is even worse and inclusion of DFT + $F_{vib}^{anharmonic}$ is absolutely essential as both DFT and DFT + $F_{vib}^{harmonic}$ find different structures to be thermodynamically more stable and *vice versa*.

Next, we show two important applications of these findings by computing the IR spectra of two test cases: (i) $Ni_4O_6(CH_4)_2$ and (ii) $Ni_4O_7(CH_4)_2$.

### 3.2 $Ni_4O_6(CH_4)_2$ cluster: harmonic IR *vs.* anharmonic IR

IR spectroscopy covers the infrared region of the electromagnetic spectrum with frequencies ranging from 4000 $cm^{-1}$ to 40 $cm^{-1}$.[74–78] In IR spectroscopy, specific frequencies are absorbed by the molecules which are characteristic of their structure. Here, we have simulated the IR spectra of one of the clusters, *viz.* $Ni_4O_6(CH_4)_2$, that are explicitly stable on including the anharmonic contribution to the free energy, to determine its characteristic vibrational normal modes. For this, we have run 8 ps *ai*MD simulation in the canonical ensemble with the Bussi–Donadio–Parrinello (BDP)[79] thermostat. From Fig. 3, we notice significant dissimilarities between the harmonic and anharmonic IR spectra of $Ni_4O_6(CH_4)_2$. Aside from the usual difference in peak intensities, the O–H stretching mode as per harmonic IR analysis near 2300 $cm^{-1}$ (see Fig. 3 upper panel) is just a negligible hump in the anharmonic IR spectrum (see Fig. 3 lower panel). Similarly, the C–H stretching mode at around 3000 $cm^{-1}$ also does not contribute to the anharmonic IR spectrum. Hence, it is evident that there is a fundamental difference in the characteristic frequencies of vibration of this structure when computed with harmonic approximation and after capturing the anharmonic effects. As a result, they contribute differently to the free energy of vibration. This makes $Ni_4O_6(CH_4)_2$ stable in the anharmonic case, but unstable under the harmonic approximation. Note that we have taken just a prototypical model system here *viz.* $Ni_4$ cluster to study its stable phases under the reactive atmosphere of $O_2$ and $CH_4$. Nevertheless, this model system is relevant and sufficient for conveying the underlying message that there is a high chance of leaving important stable phases of the catalyst while ignoring the anharmonic effects under reaction conditions.

### 3.3 $Ni_4O_7(CH_4)_2$ cluster and C–H bond activation

Apart from the above important facts, we note that incorporation of anharmonic effects helps in predicting the potential catalyst for C–H bond activation. For this, we have considered a test case, *viz.* $Ni_4O_7(CH_4)_2$ cluster, which is stable in all three cases as shown in Fig. 1a–c. We plotted its IR spectra (harmonic *vs.* anharmonic) and compared them in Fig. 4a. From Fig. 4a, we notice that O–H stretching presents significant anharmonic red-shifts in comparison to that of the harmonic case at around 273 $cm^{-1}$. These red-shift corrections lead to a change in the IR spectrum shape due to a reorganization of the vibrational modes. Primarily, we observe some remarkable dissimilarities between harmonic and anharmonic IR spectra, *e.g.*, the intensity of the C–O stretching peak has reduced significantly after the inclusion of anharmonic effects. Moreover, in the anharmonic IR spectrum, we find an intense peak at around 995 $cm^{-1}$ corresponding to the C–H bending vibration. This type of highly intense IR absorption is due to the change in dipole moment that occurs during a vibration,

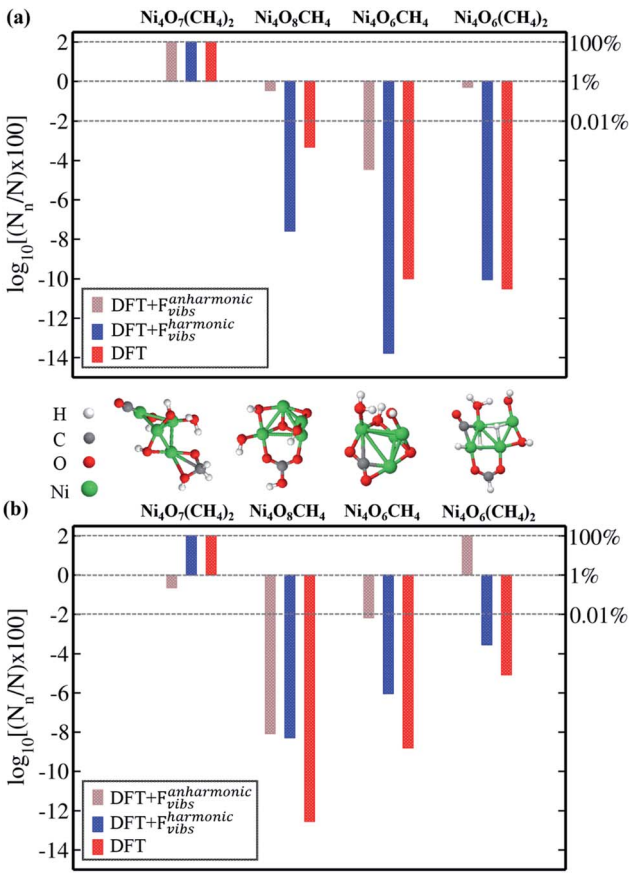


Fig. 2 Logarithm of probability of occurrence (in %) of $Ni_4O_7(CH_4)_2$, $Ni_4O_8CH_4$, $Ni_4O_6CH_4$ and $Ni_4O_6(CH_4)_2$ clusters in all three cases (DFT, DFT + $F_{vib}^{harmonic}$ and DFT + $F_{vib}^{anharmonic}$) at (a) $T = 800$ K, $p_{O_2} = 1$ atm, and $p_{CH_4} = 1$ atm, and (b) $T = 800$ K, $p_{O_2} = 10^{-10}$ atm, and $p_{CH_4} = 1$ atm.

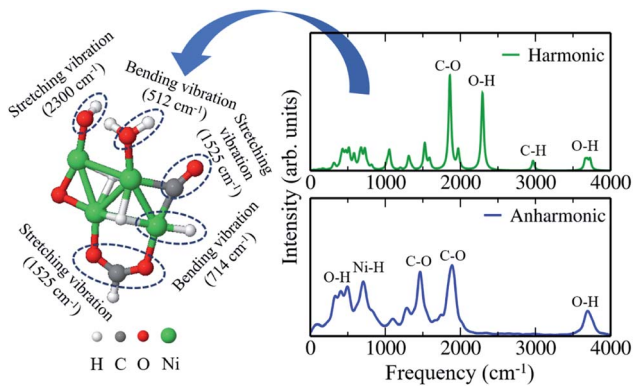


Fig. 3 Infrared (IR) spectra of $Ni_4O_6(CH_4)_2$ for both the harmonic (upper panel) and the anharmonic (lower panel) case. The possible vibrational modes corresponding to those respective peaks are also shown.

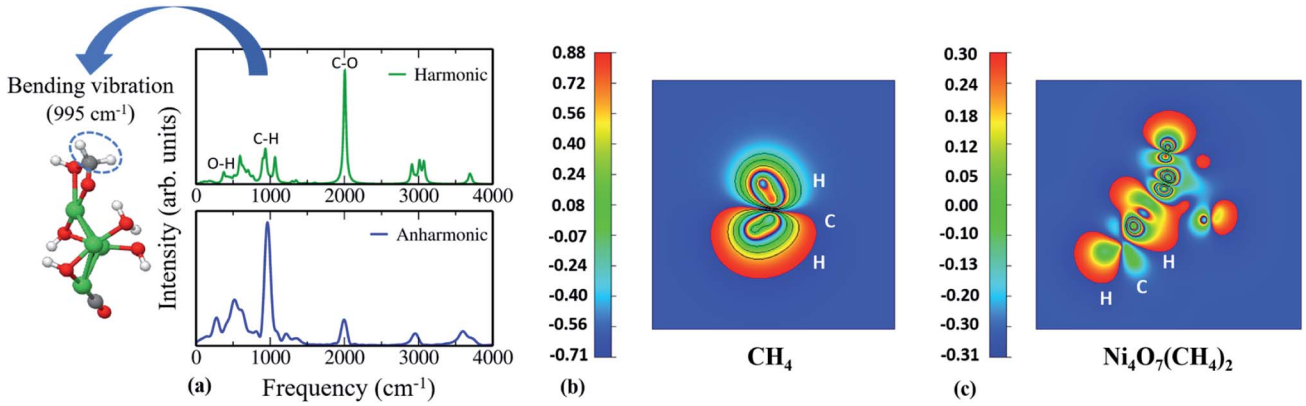


Fig. 4 (a) Infrared (IR) spectra of $Ni_4O_7(CH_4)_2$ for both the harmonic and the anharmonic case. Contour plots of electronic charge density associated with the (001) plane of (b) $CH_4$ (delocalization of charge within C–H bonds) and (c) $Ni_4O_7(CH_4)_2$ cluster (localization of charge within C–H bonds).

especially when the bond is highly polar in nature so that its dipole moment changes considerably as the bond stretches. However, the harmonic IR spectrum completely fails to capture this information. To validate this enhanced dipolar interaction in this structure, we have plotted the charge density of the $Ni_4O_7(CH_4)_2$ cluster and compared it with that of $CH_4$ (see Fig. 4b and c). To perform the charge density contour analysis, we have plotted the electron charge density for $CH_4$ and the $Ni_4O_7(CH_4)_2$ cluster for the electronic levels near the respective Highest Occupied Molecular Orbital (HOMO). The constant slicing plane is chosen such that both the C and H atoms of the C–H bond are covered. The value of electron charge density varies from a maximum (red color) to a minimum (blue color). Now, if we pay attention to the nature of the C–H bond in either case, we can clearly see the difference in charge localization. In conventional $CH_4$, the C–H bond is purely covalent, which makes it rather inert to be functionalized easily. However, in the $Ni_4O_7(CH_4)_2$ cluster, the C–H bond is very polar with the localized charge on C and H, respectively. This unusual localization of charge in the C–H bond gives rise to enhanced dipolar interactions (see Fig. 4c), and as a consequence of this, $Ni_4$ is expected to be a reliable catalyst in activating the C–H bonds in methane. It should be noted that there are indeed various other factors that also play an important part to confirm whether the catalyst is good for C–H bond activation or not and finding them needs further in-depth study through performing Nudged Elastic Band (NEB) calculations followed by kinetic Monte Carlo (kMC) simulations. But prior to that, this type of sharp peak of C–H stretching mode helps to identify possible structures for further analysis. However, if this entire analysis is done using only harmonic approximation, this stable configuration would not even be considered for C–H bond activation as its peak in the IR spectrum is pretty small and delocalized. This further confirms the importance of capturing the anharmonic contribution to this class of materials.

## 4 Conclusions

In summary, we have carried out state-of-the-art hybrid density functional theory (DFT) calculations combined with *ab initio* atomistic thermodynamics (*ai*AT) and *ab initio* molecular dynamics (*ai*MD) simulations to see how the thermodynamic stability of TM oxide clusters changes as a function of temperature and pressure ($T$, $p_{O2}$ and $p_{CH4}$). While finding the accurate thermodynamic stability, we have seen that the inclusion of anharmonicity introduces new stable phases that are entirely ignored by DFT and DFT + $F_{vib}^{harmonic}$. This has a significant impact on detecting the activation of the C–H bond, where the harmonic IR is unable to capture the correct vibrational modes. The key point that emerges out of these studies is that to understand the activation of the stable C–H bonds in methane using a metal oxide cluster as a catalyst, capturing the anharmonic effects is essential for this class of materials.

## Conflicts of interest

There are no conflicts to declare.

## Acknowledgements

P. B. acknowledges UGC, India, for the junior research fellowship [1392/(CSIR-UGC NET JUNE 2018)]. M. K. acknowledges CSIR, India, for the senior research fellowship [grant no. 09/086(1292)/2017-EMR-I]. S. B. acknowledges the financial support from SERB under a core research grant (grant no. CRG/2019/000647). P. B. acknowledges Shikha Saini for helpful discussions. We acknowledge the High Performance Computing (HPC) facility at IIT Delhi for computational resources.

## Notes and references

1 H. Prats, R. A. Gutierrez, J. J. Pinero, F. Vines, S. T. Bromley, P. J. Ramirez, J. A. Rodriguez and F. Illas, *J. Am. Chem. Soc.*, 2019, **141**, 5303–5313.
2 E. D. Goodman, A. A. Latimer, A.-C. Yang, L. Wu, N. Tahsini, F. Abild-Pedersen and M. Cargnello, *ACS Appl. Nano Mater.*, 2018, **1**, 5258–5267.

3 P. Pal, R. K. Singha, A. Saha, R. Bal and A. B. Panda, *J. Phys. Chem. C*, 2015, **119**, 13610–13618.
4 J. Su, L. Cao, L. Li, J. Wei, G. Li and Y. Yuan, *Nanoscale*, 2013, **5**, 9720–9725.
5 B. C. Enger, R. Lodeng and A. Holmen, *Appl. Catal., A*, 2008, **346**, 1–27.
6 S. H. Leenders, R. Gramage-Doria, B. de Bruin and J. N. Reek, *Chem. Soc. Rev.*, 2015, **44**, 433–448.
7 K. Aasberg-Petersen, J.-H. B. Hansen, T. Christensen, I. Dybkjaer, P. S. Christensen, C. S. Nielsen, S. W. Madsen and J. Rostrup-Nielsen, *Appl. Catal., A*, 2001, **221**, 379–387.
8 S. Das, M. Sengupta, A. Bag, M. Shah and A. Bordoloi, *Nanoscale*, 2018, **10**, 6409–6425.
9 P. Tang, Q. Zhu, Z. Wu and D. Ma, *Energy Environ. Sci.*, 2014, **7**, 2580–2591.
10 H. T. Luk, C. Mondelli, D. C. Ferre, J. A. Stewart and J. Perez-Ramrez, *Chem. Soc. Rev.*, 2017, **46**, 1358–1426.
11 Y.-X. Zhao, Z.-Y. Li, Y. Yang and S.-G. He, *Acc. Chem. Res.*, 2018, **51**, 2603–2610.
12 H.-F. Li, Y.-X. Zhao, Z. Yuan, Q.-Y. Liu, Z.-Y. Li, X.-N. Li, C.-G. Ning and S.-G. He, *J. Phys. Chem. Lett.*, 2017, **8**, 605–610.
13 H.-F. Li, Z.-Y. Li, Q.-Y. Liu, X.-N. Li, Y.-X. Zhao and S.-G. He, *J. Phys. Chem. Lett.*, 2015, **6**, 2287–2291.
14 M. Fleys, Y. Simon, D. Swierczynski, A. Kiennemann and P.-M. Marquaire, *Energy Fuels*, 2006, **20**, 2321–2329.
15 M. Gil-Calvo, C. Jimenez-Gonzalez, B. de Rivas, J. I. Gutierrez-Ortiz and R. Lopez-Fonseca, *Ind. Eng. Chem. Res.*, 2017, **56**, 6186–6197.
16 S. Bhavsar and G. Veser, *RSC Adv.*, 2014, **4**, 47254–47267.
17 D. A. Hickman and L. D. Schmidt, *Science*, 1993, **259**, 343–346.
18 D. Neumann, M. Kirchhoff and G. Veser, *Catal. Today*, 2004, **98**, 565–574.
19 A. Ashcroft, A. Cheetham, J. a. Foord, M. Green, C. Grey, A. Murrell and P. Vernon, *Nature*, 1990, **344**, 319–321.
20 S. Bhattacharya, G. Wu, C. Ping, Y. P. Feng and G. P. Das, *J. Phys. Chem. B*, 2008, **112**, 11381–11384.
21 P. D. Vernon, M. L. Green, A. K. Cheetham and A. T. Ashcroft, *Catal. Lett.*, 1990, **6**, 181–186.
22 R. C. Ramaswamy, P. A. Ramachandran and M. P. Dudukovic, *Ind. Eng. Chem. Res.*, 2007, **46**, 8638–8651.
23 Y. H. Hu and E. Ruckenstein, *Ind. Eng. Chem. Res.*, 1998, **37**, 2333–2335.
24 S. Bharadwaj and L. Schmidt, *Fuel Process. Technol.*, 1995, **42**, 109–127.
25 A. Hellman, A. Resta, N. M. Martin, J. Gustafson, A. Trinchero, P.-A. Carlsson, O. Balmes, R. Felici, R. van Rijn, J. W. M. Frenken, J. N. Andersen, E. Lundgren and H. Gronbeck, *J. Phys. Chem. Lett.*, 2012, **3**, 678–682.
26 P. M. Hundt, M. E. van Reijzen, H. Ueta and R. D. Beck, *J. Phys. Chem. Lett.*, 2014, **5**, 1963–1967.
27 A. Bhattacharya and S. Bhattacharya, *J. Phys. Chem. Lett.*, 2015, **6**, 3726–3730.
28 M. T. Reetz and W. Helbig, *J. Am. Chem. Soc.*, 1994, **116**, 7401–7402.
29 V. Sudheeshkumar, K. O. Sulaiman and R. W. Scott, *Nanoscale Adv.*, 2020, **2**, 55.
30 S. Bhattacharya, B. H. Sonin, C. J. Jumonville, L. M. Ghiringhelli and N. Marom, *Phys. Rev. B: Condens. Matter Mater. Phys.*, 2015, **91**, 241115.
31 T. M. Soini and N. Rausch, *Phys. Chem. Chem. Phys.*, 2015, **17**, 28463–28483.
32 J. Kauhler, J.-H. Chang and M.-H. Whangbo, *J. Am. Chem. Soc.*, 2005, **127**, 2277–2284.
33 E. Roduner, *Chem. Soc. Rev.*, 2006, **35**, 583–592.
34 L. Li, A. H. Larsen, N. A. Romero, V. A. Morozov, C. Glinsvad, F. Abild-Pedersen, J. Greeley, K. W. Jacobsen and J. K. Nørskov, *J. Phys. Chem. Lett.*, 2013, **4**, 222–226.
35 J. D. Aiken III and R. G. Finke, *J. Mol. Catal. A: Chem.*, 1999, **145**, 1–44.
36 C. L. Hill and C. M. Prosser-McCartha, *Coord. Chem. Rev.*, 1995, **143**, 407–455.
37 H. Guo, P. Sautet and A. N. Alexandrova, *J. Phys. Chem. Lett.*, 2020, **11**, 3089–3094.
38 H. Lee, X. Wu and L. Sun, *Nanoscale*, 2020, **12**, 4187.
39 S. Zhu, X. Lian, T. Fan, Z. Chen, Y. Dong, W. Weng, X. Yi and W. Fang, *Nanoscale*, 2018, **10**, 14031–14038.
40 D. Wang and D. Astruc, *Chem. Soc. Rev.*, 2017, **46**, 816–854.
41 A. Ruiz Puigdollers, P. Schlexer, S. Tosoni and G. Pacchioni, *ACS Catal.*, 2017, **7**, 6493–6513.
42 M. T. Greiner, L. Chai, M. G. Helander, W.-M. Tang and Z.-H. Lu, *Adv. Funct. Mater.*, 2012, **22**, 4557–4568.
43 S. Bhattacharya and G. P. Das, in *First-Principles Design of Complex Chemical Hydrides as Hydrogen Storage Materials*, Taylor and Francis Group, 2013, ch. 20, pp. 424–439.
44 S. Saini, P. Basera, E. Arora and S. Bhattacharya, *J. Phys. Chem. C*, 2019, **123**, 15495–15502.
45 P. L. Rodriguez Kessler and A. R. Rodriguez Dominguez, *J. Phys. Chem. C*, 2015, **119**, 12378–12384.
46 A. Sieber, C. Boskovic, R. Bircher, O. Waldmann, S. T. Ochsenbein, G. Chaboussant, H. U. Güdel, N. Kirchner, J. van Slageren, W. Wernsdorfer, A. Neels, H. Stoeckli-Evans, S. Janssen, F. Juranyi and H. Mutka, *Inorg. Chem.*, 2005, **44**, 4315–4325.
47 J. Ye, L. Gagliardi, C. J. Cramer and D. G. Truhlar, *J. Catal.*, 2017, **354**, 278–286.
48 S. Z. Tasker, E. A. Standley and T. F. Jamison, *Nature*, 2014, **509**, 299–309.
49 W. Keim, *Angew. Chem., Int. Ed. Engl.*, 1990, **29**, 235–244.
50 E. Monachino, M. Greiner, A. Knop-Gericke, R. Schlogl, C. Dri, E. Vesselli and G. Comelli, *J. Phys. Chem. Lett.*, 2014, **5**, 1929–1934.
51 S. De, J. Zhang, R. Luque and N. Yan, *Energy Environ. Sci.*, 2016, **9**, 3314–3347.
52 F. Li, D. R. MacFarlane and J. Zhang, *Nanoscale*, 2018, **10**, 6235–6260.
53 P. Bothra and S. K. Pati, *Nanoscale*, 2014, **6**, 6738–6744.
54 M. Andersen, C. Panosetti and K. Reuter, *Front. Chem.*, 2019, **7**, 202.
55 P. Hohenberg and W. Kohn, *Phys. Rev.*, 1964, **136**, B864–B871.
56 W. Kohn and L. J. Sham, *Phys. Rev.*, 1965, **140**, A1133–A1138.

57 S. Bhattacharya, S. V. Levchenko, L. M. Ghiringhelli and M. Scheffler, *New J. Phys.*, 2014, **16**, 123016.
58 S. Bhattacharya, S. V. Levchenko, L. M. Ghiringhelli and M. Scheffler, *Phys. Rev. Lett.*, 2013, **111**, 135501.
59 S. Bhattacharya, B. H. Sonin, C. J. Jumonville, L. M. Ghiringhelli and N. Marom, *Phys. Rev. B: Condens. Matter Mater. Phys.*, 2015, **91**, 241115.
60 K. Reuter, C. Stampf and M. Scheffler, in *AB Initio Atomistic Thermodynamics and Statistical Mechanics of Surface Properties and Functions*, ed. S. Yip, Springer Netherlands, Dordrecht, 2005, pp. 149–194.
61 A. Bhattacharya and S. Bhattacharya, *Phys. Rev. B*, 2016, **94**, 094305.
62 D. Frenkel and B. Smit, *Understanding Molecular Simulation*, Academic Press, San Diego, 2nd edn, 2002, pp. 167–200.
63 J. P. Perdew, K. Burke and M. Ernzerhof, *Phys. Rev. Lett.*, 1996, 77, 3865–3868.
64 S. Saini, D. Sarker, P. Basera, S. V. Levchenko, L. M. Ghiringhelli and S. Bhattacharya, *J. Phys. Chem. C*, 2018, **122**, 16788–16794.
65 J. Heyd, G. E. Scuseria and M. Ernzerhof, *J. Chem. Phys.*, 2003, **118**, 8207–8215.
66 J. P. Perdew, M. Ernzerhof and K. Burke, *J. Chem. Phys.*, 1996, **105**, 9982–9985.
67 V. Blum, R. Gehrke, F. Hanke, P. Havu, V. Havu, X. Ren, K. Reuter and M. Scheffler, *Comput. Phys. Commun.*, 2009, **180**, 2175–2196.
68 E. v. Lenthe, E. J. Baerends and J. G. Snijders, *J. Chem. Phys.*, 1993, **99**, 4597–4610.
69 A. Tkatchenko and M. Scheffler, *Phys. Rev. Lett.*, 2009, **102**, 073005.
70 N. S. Martys and R. D. Mountain, *Phys. Rev. E: Stat. Phys., Plasmas, Fluids, Relat. Interdiscip. Top.*, 1999, **59**, 3733–3736.
71 D. J. Evans and B. L. Holian, *J. Chem. Phys.*, 1985, **83**, 4069–4074.
72 E. Arora, S. Saini, P. Basera, M. Kumar, A. Singh and S. Bhattacharya, *J. Phys. Chem. C*, 2019, **123**, 62–69.
73 S. Bhattacharya, D. Berger, K. Reuter, L. M. Ghiringhelli and S. V. Levchenko, *Phys. Rev. Mater.*, 2017, **1**, 071601.
74 B. Stuart, in *Infrared Spectroscopy*, American Cancer Society, 2015, pp. 1–18.
75 W. Z. Weng, M. S. Chen, Q. G. Yan, T. H. Wu, Z. S. Chao, Y. Y. Liao and H. L. Wan, *Catal. Today*, 2000, **63**, 317–326.
76 V. L. Sushkevich, R. Verel and J. A. van Bokhoven, *Angew. Chem., Int. Ed.*, 2020, **59**, 910–918.
77 S. Fouladvand, M. Skoglundh and P.-A. Carlsson, *Catal. Sci. Technol.*, 2014, **4**, 3463–3473.
78 X. Wang, N. M. Martin, J. Nilsson, S. Carlson, J. Gustafson, M. Skoglundh and P.-A. Carlsson, *Catalysts*, 2018, **8**, 545.
79 J. Ruiz-Franco, L. Rovigatti and E. Zaccarelli, *Eur. Phys. J. E: Soft Matter Biol. Phys.*, 2018, **41**, 80.